Nanoscale

Accepted Manuscript

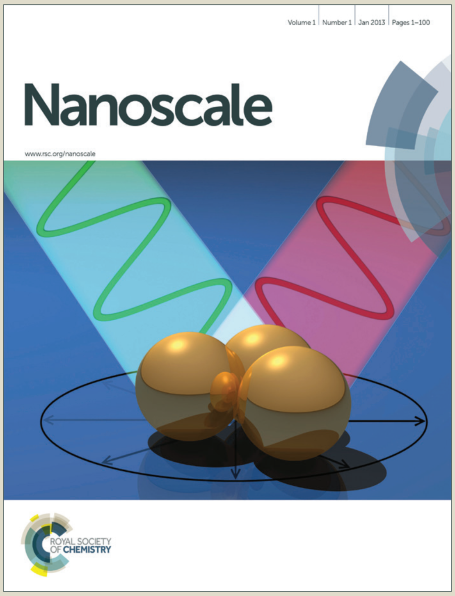

ROYAL SOCIETY OF CHEMISTRY

www.rsc.org/nanoscale

Tunable Multiferroic and Bistable/Complementary Resistive Switching Properties of Dilutely Li – Doped $BiFeO_3$ Nanoparticles: An Effect of Aliovalent Substitution

Mandar M. Shirolkar[1], **Changshan Hao**[2], **Xiao Lei Dong**[2], **Ting Guo**[2], **Lei Zhang**[2], **Ming Li**[2] **and Haiqian Wang**[*]

Hefei National Laboratory for Physical Sciences at the Microscale, University of Science and Technology of China, Hefei, Anhui 230026, People's Republic of China.

Abstract

We report the potential way to enhance and tune the multiferroic and resistive switching properties of $BiFeO_3$ nanoparticles through the dilute aliovalent Li^{1+} doping (0.046 atomic percent) at the Fe^{3+} site of $BiFeO_3$. The high purity of samples and extent of dopant were confirmed by different physical characterizations. The enhanced multiferroic properties with magnetic moment per Fe atom ≈ 0.12 μ_B and electric polarization ≈ 49 $\mu C/cm^2$ was observed in Li^{1+} doped sample. The phenomenological model has been proposed to support the observed magnetic behavior of doped samples. From the potential application point of view, we further report, doping concentration and the polarization coercivity dependent highly stable resistive switching behavior (endurance cycles > 10^3 and stability > 10^6 s) of Li – doped $BiFeO_3$ nanoparticles. The stable complementary resistive switching behavior (1-bit operation) for > 50 cycles and under voltage pulse for 10^3 cycles in the doped $BiFeO_3$ at low operating bias is reported. Thus, dilute aliovalent Li^{1+} doping enables the tunability in the ferroic and resistive switching properties of $BiFeO_3$ and show promising multiferroic material.

Keywords: Aliovalency, ferromagnetism, exchange bias, magnetoelectric, resistive switching

---

[1] mandar@ustc.edu.cn, mmshirolkar@gmail.com

[2] The authors have contributed equally to the work.

[*] Corresponding Author: hqwang@ustc.edu.cn

1. Introduction

Magnetoelectric multiferroic bismuth ferrite ($BiFeO_3$ or BFO) has gained considerable attention in recent years, because of its promising industrial applications and underlying fascinating science [1 – 7]. In comparison with the intrinsic single – phase $BiFeO_3$, their composite and doped counterparts are reported to demonstrate a significantly higher multiferroic properties, which enable their use for the fabrication of multifunctional devices [8 – 16].

The doping or chemical substitution is an approach, which enables the substitution of dopant at Bi or Fe or O site [13]. This technique has been extensively reported as a method to improve the multiferroic properties of BFO, which results in the observation of net magnetization, improvement in the ferroelectric behavior, resistivity and reduction in the leakage current [19 – 36]. Among the several doping attempts, isovalent and aliovalent dopants at the cationic site have been reported. At the Bi – site the isovalent dopant substitution leads to the structural changes, through imbalance in $6s^2$ lone pair, which affect the ferroelectric behavior of BFO and moderately affecting the magnetism. On the other hand, substitution at the Fe – site directly affects magnetic behavior without or weakly affecting the ferroelectric behavior of material [13, 20 – 31]. While few approaches have reported aliovalent or nonisovalent substitution at cationic sites (Bi or Fe) [13, 28 – 36]. Such an aliovalent doping leads to either variations in the cation valence, filling of the intrinsic oxygen vacancies or creation of cation vacancies [22, 23, 37]. Thus, it has been observed that aliovalent doping drastically enhances the multiferroic properties of BFO. While, to the best of our knowledge no reports are available on the multiferroic properties of Li – doped $BiFeO_3$. The selection of dopant ion was based on the facts that (i) Li^{1+} being highly aliovalent compared to other cations Bi and Fe and (ii) the intriguing properties reported in the lithium doped other nanomaterials, which include semiconductors, magnetic, multiferroic materials etc. [38 – 41]. Hence, it is expected that Li^{1+} doping could significantly affect the multiferroic properties of BFO and enable its potential use in the device applications such as memristor.

In the recent years, memristor or resistive switching (RS) properties have been observed in several materials [42 – 45]. The resistive switching is an important phenomenon, which can be utilized to fabricate the high – density nonvolatile memory devices [42, 44]. The low operating voltage, fast switching activity, endurance, retention and temperature dependent stabilities are the major parameters for the resistive switching devices [43, 45]. The BFO can be a good candidate for the resistive switching device compared to the reported materials due to its interesting multiferroic properties and capability to tune the leakage current [36, 46]. In the epitaxial thin films, single crystals and the nano – islands of BFO, the RS was observed to be driven by the ferroelectric properties and shows switchable diode effects [47 – 49]. While in the polycrystalline thin films of BFO the RS was observed to be independent of forming voltage [50]. It has been also observed that the doping can improve the RS properties of BFO by tuning multiferroic properties and the leakage current [36, 46, 51, 52]. Due to aliovalency of lithium, the Li^{1+} doping in BFO lattice can drastically influence the multiferroic properties, defect states, leakage current and hence the RS behavior of BFO.

In this paper, we report following important results: (i) an enhancement in the magnetic moment per Fe atom ($\approx 0.12\ \mu_B$) was observed for 0.046 atomic percent Li^{1+} doping concentration. The results has been qualitatively explained on the basis of the proposed phenomenological model, (ii) enhancement in the electric polarization ($\approx 49\ \mu C/cm^2$) was observed, (iii) doped samples show strong magnetoelectric coupling compared to pure BFO, (iv) doping concentration dependent stable bistable and complementary resistive switching (BRS and

CRS) was observed in the doped samples. The electroforming process of the devices shows possible correlation with the observed polarization properties. We empirically proposed an insight to improve the multiferroic and resistive switching characteristics of $BiFeO_3$ nanoparticles.

2. Experimental

In this paper, we report the synthesis of high quality pure i.e. undoped and Li^{1+} doped $BiFeO_3$ nanoparticles. We have exploited soft chemical sol – gel route in combination with mild hydrothermal treatment for the preparation of samples (see supporting information for details). The molar concentration of lithium precursor, $LiNO_3$ for doping Li in the $BiFeO_3$ structure was 0.2, 0.4 and 0.6 mole %. The as prepared nanoparticles were characterized with various physical characterizations to evaluate purity and extent of Li doping and the effect of doping on the properties of BFO. It includes atomic absorption spectroscopy (AAS), X – ray diffraction (XRD), Raman spectroscopy, transmission electron microscopy (TEM), X – ray photoelectron spectroscopy (XPS), differential scanning calorimetry (DSC), field dependent (M – H) and temperature dependent (M – T) magnetic measurements, Mössbauer measurement, electric polarization, magnetocapacitance measurement and resistive switching (see supporting information for details).

3. Results and discussion

Purity and actual percentage of Li in $BiFeO_3$ samples is determined by AAS. The study shows that the actual atomic percentage (average) of lithium in all the doped $BiFeO_3$ samples is 0.01 ± 0.02 %, 0.027 ± 0.02 % and 0.046 ± 0.01 %. Hereafter throughout the discussion 0 (pure), 0.01, 0.027 and 0.046 % lithium doped BFO samples are termed as B_1, B_2, B_3 and B_4 respectively.

The Rietveld refined XRD patterns of all the samples are shown in Figure 1. We observed that all the diffraction peaks are matched well with the rhombohedral structure of pure $BiFeO_3$ ($R3c$ space group, JCPDS file no. 71 – 2494) [53]. The pattern clearly indicates the absence of any kind of impurity phases. This shows the proper incorporation and dispersion of Li^{1+} ions into the $BiFeO_3$ matrix up to doping concentration of 0.046 at. %. The structural parameters obtained from the refinement for pure and doped samples are given in Table 1. The structural parameters of sample B_1 are reasonably close to the reported values in the literature [15, 54]. On the other hand, the drastic changes were observed in the structural parameters after Li doping in $BiFeO_3$ (see Table 1). The lattice parameters decrease with the reduction in unit – cell volume as Li doping concentration increases. The decrement in the structural parameters can be explained on the basis of Goldschmidt tolerance factor (t) which is associated with the cationic size variation (Shannon ionic radii) between A and B ions [55 – 57]. In the present case t value for B_1 was observed to be 0.9682 and represent $a^-a^-a^-$ (Glazers notation) anti – phase tilted perovskite system, while Li^{1+} doped samples show $t = 0.9678$, 0.9667 and 0.9656 for B_2, B_3 and B_4 samples respectively. It shows that doped samples exhibit anti – phase tilting, but with changes in the octahedral tilting.

The XRD analysis shows, $BiFeO_3$ unit cell volume undergoes compression due to doping in which Fe^{3+} is substituted by Li^{1+}. The substitution of Li^{1+} ion into a Fe^{3+} site of perovskite structure reduces positive charge according to the reaction describe as follows:

$$\frac{1}{2}Bi_2O_3 + Li_2O \rightarrow (Bi_{Bi})^x + 3(Li_{Fe})^\bullet + O_\circ^x + \frac{1}{4}O_2 + 3e^- \qquad (1).$$

Thus, changes in the lattice parameters will arise due to both the Li – substitution and the defect that were created due to charge compensation. The charge compensation can be attained through various compensation mechanisms, each of them perhaps have a balanced effect on the cell parameters such as ionic radius misfit, electrostatic repulsive forces and octahedron tilting. In addition to that Li^{1+} may not be homogeneously distributed in the $BiFeO_3$ matrix. Hence, we can expect that charge compensation can also be from the local concentration of the dopant.

We observed that Fe – O bond length and Fe – O – Fe bond angle decreases, which is expected since (i) oxidation states of dopant and host site are different and (ii) the effective ionic radius of Li^{1+} (0.76 Å) is higher than Fe^{3+} (0.645 Å) in the octahedral coordination [55]. It buckles or modulates the FeO_6 octahedra, as a consequence Fe ions come closer to each other.

To quantify the octahedral changes in the unit cell, we have obtained reciprocal space electron density of unit cell. The two dimensional reciprocal space electron density of unit cell obtained from the refinement is shown in Figure 2. We observed that the sample B_1 exhibit electron density similar to that reported earlier [15]. While, doped samples B_2 – B_4 shows doping induced distortion i.e. buckling in the FeO_6 octahedra. It was observed that doping increases interactions between octahedra. It enhances the superexchange interaction between the two nearest Fe ions through oxygen ions and indicates lattice strain induced changes in the magnetic properties of $BiFeO_3$ [15].

We also observed that doped samples show variation in the *c/*a ratio and the increase in the Bi – O bond length and O – Bi – O bond angle compared to undoped BFO, which shows the variation in the ferroelectric features [8]. The observed results strongly show that the ferroelectric features of doped BFO are also affected due to dilute Li – doping. In order to further, confirm the observed structural changes Raman measurement was carried out on these samples.

Raman spectroscopy of samples is shown in Figure 3. The measured Raman spectra of all the samples were fitted and decomposed into its individual Lorentzian components. It shows 13 characteristic Raman modes ($4A_1 + 9E$) reported for $BiFeO_3$ having rhombohedral $R3c$ space group [15, 58]. The observed Raman modes are deconvoluted and are listed in Table 2. In our samples, the absence of Raman modes due to impurity phases supports XRD data. The first principle calculation suggests that Bi atoms contribute low frequency modes below 167 cm^{-1}, Fe atoms mainly participate in the modes between 152, 262 cm^{-1} and in higher frequency modes, while above 262 cm^{-1} modes from oxygen atoms are dominated [59, 60]. It is known that Raman spectra are sensitive to atomic displacements. Hence, the modifications in Raman modes due to Li^{1+} substitution in BFO lattice can provide valuable information. We observed some modifications in the Raman spectra due to doping of Li at Fe site, (i) the Raman modes for BFO show the red shift i.e. shifting towards higher wavenumber after doping, (ii) the modes $A_1 - 1$ and $A_1 - 2$ shows the large red shift, a monotonic enhancement in the intensity and the broadening, which show changes in the magnetic and ferroelectric properties of BFO due to doping. The observed results could be attributed to (a) the lower mass of Li (6.94 g/mol) compared to Fe (55.85 g/mol) indicating that the dopant Li is entered into the Fe site of $BiFeO_3$, (b) lattice disorder and (c) variation in t value due to doping.

Interestingly, on close observation of different phonon modes, in the doped samples we observed a softening in the magnitude of E modes centered around 262 and 350 cm^{-1} (shown as inset in Figure 3). It can be attributed to motion of oxygen, which produces substantial destabilization in the FeO_6 octahedral chains and affect the octahedral rotation [61, 62]. The high pressure Raman study on BFO have reported similar softening of E – modes and attributed to the modulation in the FeO_6 local environment due to an applied high pressure. These modes are closely associated with the vibration of Fe – O bond. Thus, it indirectly relates to the possible changes in the Fe – O related structural parameter and the modifications in magnetic properties [62, 63].

Thus, it could be seen from the XRD and Raman measurements that Li^{1+} doping significantly distort the BFO lattice. If we compared the observed structural changes with the reported work on aliovalently doped $BiFeO_3$ [28 – 36], then it was realized that in our case the doping concentration is relatively low. However, BFO lattice undergoes large structural distortion even at low doping concentration, which could be attributed to high aliovalency of Li compared to Bi and Fe. The other physical characterizations XPS and Mössbauer spectroscopy shows that Li^{1+} has not altered the charge state of either Fe or Bi (see supplementary information).

Figure 4 shows TEM of undoped and doped $BiFeO_3$ nanoparticles. The undoped BFO exhibit nearly spherical morphology, while nearly no change in the morphology was observed for the doped samples. The particle size in the case of doped samples was observed to be smaller than undoped sample. The average particle size determined from TEM micrographs are 45 nm for B_1, 38 nm for B_2, 30 nm for B_3 and 24 nm for B_4. The high-resolution TEM micrographs further shows that the particles exhibit core – shell like structure. The shell of particles in all the cases is having less crystallinity compared to the core. The average shell thickness of the order of $\approx 2 \pm 2$ nm was observed in B_1, while doped samples show the shell thickness $\approx 4 \pm 2$ nm. Thus, shell of particles exhibit defects and could contribute to the behavior of particles.

The structural and calorimetric measurements (see supplementary information) reveal the changes in the magnetic properties of material. To quantify it it room temperature magnetic measurements were carried out. Figure 5 shows the room temperature M – H study on the undoped and Li – doped $BiFeO_3$ nanoparticles. The first (upper) inset in Figure 5 shows magnified view of the M – H loops representing coercivity. It can be seen that all the samples exhibit unsaturated M – H loop and weak coercivity. The sample B_1 exhibits magnetic moment per Fe atom (μ_B/Fe) ≈ 0.026 and the appreciable coercivity ≈ 410 Oe. In case of doped samples, the maximum μ_B/Fe ≈ 0.12 was observed in the sample the B_4. While, coercivity in the doped samples was observed to be remain constant ≈ 132 Oe (nearly) with an increase in the doping concentration. The variation of magnetic parameters with the doping concentration is shown as an inset in Figure 5 (see second (lower) inset). The observed magnetic properties in the undoped and doped samples represent the presence of interparticle dipole – dipole and the exchange interactions i.e. reduction in the antiferromagnetic superexchange interactions due to suppression of spin cycloid, which gives rise to the Dzyaloshinksii – Moriya (DM) interaction due to reduction in the particle size and leads to spin canting [64]. This spin canting induces competing interactions between antiferromagnetic and ferromagnetic exchange components, which leads to weak ferromagnetism. In the case of doped samples, in addition to above mechanism, the structural distortion which is evidenced from the XRD and Raman measurements modulates Fe – O bond lengths, Fe – O – Fe bond angles and FeO_6 octahedra, which also contribute in the DM interaction and the spin canting. Hence, the magnetization in the doped samples is higher compared to undoped sample. Moreover, the magnetization observed in the all the samples can be explained on the basis of Nèel theory of antiferromagnetism [65, 66]. According this theory, in case of antiferromagnetic nanoparticles the role of surface in the magnetic behavior of material becomes important due to increase in the surface – to – volume ratio, which controls the magnetic behavior of the material. The antiferromagnetic nanoparticles consist of two sublattices: spin up and spin down. At the surface the imbalance in the number of spins between these two sublattices give rise to magnetic moment in the antiferromagnetic nanoparticles.

Nearly, linear dependent relation between saturation magnetization vs. 1/d (data not shown) and the splitting observed in the ZFC – FC curve (see supporting information) show that all the samples exhibit antiferromagnetic core and ferromagnetic shell supporting TEM studies [64, 67]. The results also show that although the spiral spin structure is suppressed in the samples through the variation in the particle size and the rotation of the FeO_6 octahedron, the intrinsic antiferromagnetic interaction still occurs in the nanoparticles [64, 67]. Interestingly, we observed that the M – H curve in both the cases shift towards the negative axis (see first (upper) inset in Figure 5), indicating exchange bias features, as described above it arises due to exchange coupling interactions between antiferromagnetic core having collinear spins and ferromagnetic surface with canted spins [68 – 71]. The inverse correlation was observed between exchange bias field and doping concentration (see second (lower) inset in Figure 5). The observed decrement in the coercivity and an exchange bias field in the doped samples show the transformation of a long – range spin cycloid of $BiFeO_3$ to a collinear antiferromagnetic spin structure. The observed results are primarily attributed to the decrement in the size of nanoparticles resulted due to Li^{1+} doping in Fe site. It could lead to the modulation of the local spin canting. Similar observation has been reported by Sosnowska et al. in Mn doped $BiFeO_3$ [72]. However, the doping concentration reported by Sosnowska et al. was comparatively higher than ($x = 0.2$) than the current work ($x = 0.046$ at. %). Thus, it could be reasonable to postulate that low concentration of aliovalent Li^{1+} doping at Fe site decreases the particle size, which subsequently modulates the spin cycloid of $BiFeO_3$. This observation can be useful from the device application point of view.

Additionally, we proposed a following phenomenological qualitative model to explain the observed magnetic properties. Figure 6 schematically shows possible mechanisms for the ferromagnetism in the sample. The undoped sample exhibit magnetic properties as shown in

Figure 6 (A) and (B) and can be explained on the basis of the models as discussed above. On the other hand, being magnetically inactive, Li^{1+} ions cannot contribute directly to the nonzero remanent magnetic moment. However, time to time spatial replacement of certain magnetically active Fe^{3+} ions with nonmagnetic Li^{1+} ions that can perturb or completely suppress the spatial spin cycloid (see Figure 6(C)). Alternatively, if we consider intrinsic AFM ordering arising from Fe^{3+} - O^{2-} - Fe^{3+} interactions, then by replacing Fe^{3+} time to time by Li^{1+} allows to ferromagnetic – like coupling rather than antiferromagnetism as illustrated in Figure 6(D). This type of oxygen mediated coupling straightened the Fe – O – Li bond angle and length. Thus, through this model we suggest that higher the ordering between Fe^{3+} and Li^{1+} the larger should be the magnetizations.

The changes observed in Bi – O structural parameters and in the Curie temperature (see supporting information) due to aliovalent Li^{1+} doping also suggest that the ferroelectric properties are also affected. To quantify it the ferroelectric properties of all the samples investigated by the P – E loop measurements. Figure 7 shows P – E hysteresis loops of undoped and doped BFO samples. The undoped BFO shows ferroelectric nature however with reasonably high lossy characteristic [8, 14, 17, 73, 74]. While, all the Li^{1+} - doped BFO nanoparticles exhibited better polarization properties compared to undoped sample. The variation of polarization properties with a doping concentration is shown as an inset in Figure 7. The sample B_4 shows highest polarization properties with $P_s = 49$ μC/cm^2, $P_r = 28$ μC/cm^2 and $E_c = 442$ V/cm. The observed polarization properties conclude that Li^{1+} doping enhances ferroelectric properties of $BiFeO_3$.

Overall, considering the effect of dilute dopant on the properties of $BiFeO_3$ nanoparticles, it can be observed that multiferroic properties significantly improved by doping a tiny amount of aliovalent Li in BFO lattice. It is interesting to note that the enhancement in the properties was observed without altering the crystal symmetry. In the doped sample B_4, the magnetic moment per Fe atom and the saturation polarization was observed to be nearly four and eight orders of magnitude higher compared to pure $BiFeO_3$ respectively.

Based on the above characterizations we further constructed prototype device using B_1 to B_4 samples. A Schematic configuration of the Ag/$BiFeO_3$ or $BiFeO_3$: Li/Cu device with I – V measurement setup is shown in Figure 8(A). Interestingly, the electroforming process, which drive the devices constructed with B_1, B_2, B_3 and B_4 in the RS states were observed to be coercive field value (E_c) observed in the sample from the polarization measurements. Typical I – V curve of the devices for consecutive ten cycles is shown in Figure 8(B). It can be observed that device demonstrate well – defined clockwise symmetrical BRS processes. The sweeping sequence of an applied bias is shown in Figure 8(B) with arrow marks. By gradually increasing the positive voltage, the resistance changes from LRS to HRS, which is RESET process of the device. This process was also observed to be doping concentration dependent, for B_1: ≈ + 3.3 V, B_2: ≈ + 3.0 V, B_3: ≈ + 1.9 V and B_4: ≈ + 0.5 V. Subsequently, as the applied bias swept from zero to negative values, a reverse SET process was also observed for B_1: ≈ - 3.3 V, B_2: ≈ - 3.0 V, B_3: ≈ - 1.9 V and B_4: ≈ - 0.5 V. The BRS behavior of undoped sample is in agreement with the previously reported work [46, 47]. On the other hand, in the doped samples resistive switching show possible correlation between dopant concentration and BRS processes.

It was observed that in the sample B_4 BRS process is readily achieved at an applied bias of ± 0.5 V, which has potential significance from the memory device point of view, operating at low bias. From the paradigm memory device point of view, the endurance and retention properties of the Ag/B_4/Cu device were evaluated at room temperature. As shown in Figure 8(C), the device shows relatively stable endurance of BRS states for > 10^3 cycles and reasonably no significant change in the magnitude of resistance value for > 10^6 s (see Figure 8(D)). Though, slight degradation of BRS states were observed over the operation conditions, the excellent endurance and retention properties of Ag/$BiFeO_3$:Li/Cu device confirm their potential application in the memory devices.

More interestingly, the behavior of the device constructed with the sample B_4 shows that it could be used for complementary resistive switching device purpose (see Figure 8(E)). We demonstrate it for 1-bit operation in the following way. After the electroforming process, the as prepared device was switched to the electroformed state in LRS mode. Further, by applying - 0.5 V, the device was switches to HRS (denoted as H_O). Consequently, when the applied voltage was swept in a sequence of 0 V → - 0.5 V → 0 V → + 0.5 V → 0 V, the device shows a four – phase resistive switching processes with a high degree of repeatability and stability (denoted as ① – ④). It can be seen from Figure 8(E) that: (i) with the increase in the applied voltage under positive bias, the device shows linear behavior, while in the proximity to a threshold voltage ≈ - 0.25 V (V_1) the device switches into the LRS (ON) state. (ii) With further rise in the negative bias current drop occurs at another threshold voltage ≈ - 0.5 V (V_2) then, the device was switched to HRS state (H_1). (iii) As applied voltage reached a positive threshold voltage ≈ + 0.25 V (V_3) the device was once again switched from H_1 to LRS (ON) state, which remain in that state until relatively high positive threshold voltage ≈ + 0.5 V (V_4). Further, H_1 state was upheld in the device in the proximity of the negative voltage range of ≈ - 0.5 V (V_3). (iv) The device was returned again to H_O state when $V > V_4$. Here, H_O and H_1 can be regarded as the '0' and '1' states of the device respectively. These states can be distinguished by the applications of a read voltage V into the range $V_3 < V < V_4$. In the present case, H_O is kept in the HRS state, while H_1

is switched to LRS i.e. ON state. The erase operation (i.e. 0) can be realized by applying the voltage $V > V_4$ and write operation (i.e. 1) by the application of a voltage $V < V_2$. On the contrary, if H_O and H_1 is defined as ‘1’ and ‘0’ states of the device respectively. Then in that case the read voltage should follow the condition $V_1 < V < V_2$, with an erase voltage $V < V_2$ and write voltage $V > V_4$. The nearly symmetrical resistive switching behavior of the device shows that ohmic – like contact formation within the device. In most of the cases, the process or the feature observed at high bias condition (here ± 0.5 V) can be either attributed to electromigration of dopant ions or Joule heating effect [42, 43, 75]. The CRS process was observed to be stable for consecutive 50 cycles. The observed four – level switching process nature is analogous to the reported anti – serially stacked CRSs [76]. Since in HRS state at low bias condition in CRS cells both ‘0’ and ‘1’ stored, the device permits the ability of suppressing the crosstalk and high power consumption variability issues associated with crossbar array configuration [42, 76].

From the point of view of real memory devices, BRS/CRS by pulses is necessary. Figure 8(F) shows RS achieved by voltage pulses. The resistance values were read at 0.25 V. As shown in Figure 8(F), we obtained bistable on/off i.e. one bit switching by applying a voltage + 0.5 V for 50 ns for SET process and – 0.5 V for 100 µs for RESET process. The device shows reasonably stable CRS process for 10^3 cycles at an applied pulse condition. Thus, it was suggested that Li^{1+} doped $BiFeO_3$ nanoparticles can serve as a promising candidate for future memory device applications.

The observed resistive switching behavior of the undoped and doped $BiFeO_3$ nanoparticles sandwiched in the two electrodes is attributed to the oxygen vacancy mediated filamentary conduction phenomenon. In the present case, the possible ways of formation of oxygen vacancies and defects are (i) the defects observed at the particle boundary, which gave rise to core – shell like structure could take part in the oxygen vacancy mediated filamentary conduction [42 – 45, 75], (ii) the partial oxidation of electrode surfaces during the electroforming process, which are in contact with BFO could develop an interface insulating layer (IIL), which can introduce oxygen related defects in BFO. The IIL formation within the device is evident from the exponential nature of the resistive cycle [77] and (iii) the local Joule heating effect in the device during the electroforming process.

The reports on BRS shows that it can be well demonstrated through oxygen vacancy mediated tunneling or non – linear transport barriers [78, 79]. With the application of a voltage across the device, the electronic conduction in these devices through such a barrier can be achieved through the motion of oxygen vacancies. The oxygen vacancies formed during the electroforming process can be described through Kröger – Vink notation as described below:

$$O_O \rightarrow \frac{1}{2}O_2 \uparrow + V_O^{\bullet\bullet} + 2e^- \qquad (2)$$

Where O_O and $V_O^{\bullet\bullet}$ represent lattice oxygen ions and oxygen vacancies respectively.

Subsequently, we also pointed out that BFO is ferroelectric. Hence, we could not completely exclude the effect of electric polarization on observed BRS. In single crystal BFO and epitaxial BFO thin film the intrinsic bulk polarization can induce the diode – like behavior [47, 48, 80]. However, in the present case, the thin film composed of nanoparticles, which are polycrystalline in nature. The particular relationship between the electric polarization and the transport property is difficult due to the presence of a large number of grain boundaries, which govern the transport property.

The comparison of current work with the literature on RS properties of aliovalently doped BFO shows that in our case RS properties exhibit strong dopant concentration dependence [36, 46, 52]. Though samples were polycrystalline in nature, the RS could be readily achieved at relatively lower operating voltages. The results also show the principle role of Li^{1+} dopant at Fe^{3+} site, which stimulates precise incorporation of oxygen vacancies in an intrinsic way. We also proposed that to understand exact correlation between electric polarization and resistive switching further experimental and theoretical work is necessary.

We have also checked the stability of the BFO nanoparticle coating against the mechanical wear and tear, simply by scratching it. We observed that the film is not much stable against mechanical force and can simply peel off from the substrate.

At the end, we have shown that nonmagnetic aliovalent Li^{1+} doping in $BiFeO_3$, preliminary affects the magnetic properties of the BFO, while changes observed in the ferroelectric properties of $BiFeO_3$ are lattice strain driven and due to intrinsic multiferroicity. The ferroelectric polarization induced resistive switching feature observed in doped BFOs can act as a promising candidate for resistive switching based devices. We further proposed that at higher Li^{1+} concentration the effect of aliovalency will be more noticeable and can significantly affect the multiferroic and ferroelectric property driven resistive switching properties of BFO. In addition, the host matrix oxygen stoichiometry will get affected after doping that will also contribute in the multiferroic behavior of the material. To understand the complete mechanism additional experimental and theoretical work is necessary.

4. Conclusion

In summary, $BiFeO_3$ nanoparticles have been successfully synthesized through a combination of chemical sol – gel and hydrothermal methods followed by heat treatment. The average particle size observed between 25 – 35 nm. The structural measurements preliminary showed that dilute Li^{1+} doping induces large structural distortion in the parent $BiFeO_3$ structure, it can be attributed to aliovalency of dopant atom and lattice defects. The variation of Li^{1+} dopant concentration alters the magnetic and ferroelectric properties of $BiFeO_3$ to different extents. Through M – H measurements it was observed that nanoparticles show room temperature weak ferromagnetic nature, exchange bias phenomenon and frustrated magnetic behavior due to aliovalent doping. The behavior was attributed to the coexistence of canted spin structure and oxygen ion mediated Fe – Fe interactions and core – shell structure having antiferromagnetic core and ferromagnetic shell. A phenomenogical model has been proposed for the observed magnetic nature. The doped material showed relatively less lossy, enhanced ferroelectric behavior and good magnetocapacitance properties compared to undoped $BiFeO_3$. The ferroelectric properties mediated reasonably stable bistable resistive switching was observed in the undoped and doped samples. The doped samples show relatively lower switching voltage than pure $BiFeO_3$, which enable their potential use in the complementary resistive switching based memory device applications. Thus, by appropriately varying Li^{1+} doping concentration in $BiFeO_3$ nanoparticles led to better material for various potential device applications.

Acknowledgement

MMS thanks Dr. J. Rodríguez-Carvajal (Laboratoire Léon Brillouin (CEA-CNRS), CEA/Saclay, 91191 Gif-sur-Yvette Cedex, France) for the help during Rietveld refinement.

References

1. H. Schmid, *Ferroelectrics*, 1994, **162**, 19 – 25.
2. W. Eerenstein, N. D. Mathur and J. F. Scott, *Nature*, 2006, **442**, 759 – 765.
3. N. A. Hill, *J. Phys. Chem B*, 2000, **104**, 6694 – 6709.
4. N. A. Hill and A. Filippetti, *J. Magn. Magn. Mater.*, 2002, **242 – 245**, 976 – 979.
5. C. – W. Nan, M. I. Bichurin, S. Dong, D. Viehland and G. Srinivasan, *J. Appl. Phys.,* 2008, **103**, 031101.
6. M. M. Vopson, *J. Phys. D: Appl. Phys.*, 2013, **46**, 345304.
7. J. F. Scott, *J. Mater. Chem.*, 2012, **22**, 4567 – 4574.
8. G. Catalan and J. F. Scott, *Adv. Mater.*, 2009, **21**, 2463 – 2485.
9. S. Picozzi and C. Ederer, *J. Phys.: Condens. Matter*, 2009, **21**, 303201.
10. J. Silva, A. Reyes, H. Esparza, H. Camacho and L. Fuentes, *Integr. Ferroelectr.*, 2011, **126**, 47 – 59.
11. Y. Mao, T. –J. Park and S. S. Wong, *Chem. Comm.*, 2005, **46,** 5721 – 5735.
12. C. N. R. Rao, A. Sundaresan and R. Saha, *J. Phys. Chem. Lett.*, 2012, **3**, 2237 – 2246.
13. C. – H. Yang, D. Kan, I. Takeuchi, V. Nagarajan and J. Seidel, *Phys. Chem. Chem. Phys.*, 2012, **14**, 15953 – 15962.
14. J. Wang, J. B. Neaton, H. Zheng, V. Nagarajan, S. B. Ogale, B. Liu, D. Viehland, V. Vaithyanathan, D. G. Schlom, U. V. Waghmare, N. A. Spaldin, K. M. Rabe, M. Wuttig and R. Ramesh, *Science*, 2003, **299**, 1719 – 1722.
15. M. M. Shirolkar, R. Das, T. Maity, P. Poddar and S. K. Kulkarni, *J. Phys. Chem. C*, 2012, **116**, 19503 – 19511 and references therein.

16. S. M. Yusuf, P. K. Manna, M. M. Shirolkar, S. K. Kulkarni and G. K. Dey, *J. Appl. Phys.*, 2013, **113**, 173906.
17. S. N. Tripathy, B. G. Mishra, M. M. Shirolkar, S. Sen, S. R. Das, D. B. Janes and D. K. Pradhan, *Mater. Chem. Phys.*, 2013, **141**, 423 – 431.
18. A. Singh, V. Pandey, R. K. Kotnala and D. Pandey, *Phys. Rev. Lett.*, 2008, **101**, 247602.
19. I. Apostolova and J. M. Wesselinowa, *J. Magn. Magn. Mater.*, 2009, **321**, 2477 - 2482.
20. J. Bielecki, P. Svedlindh, D. T. Tibebu, S. Cai, S. –G. Eriksson, L. Borjesson and C. S. Knee, *Phys. Rev. B*, 2012, **86**, 184422.
21. D. P. Dutta, B. P. Mandal, R. Naik, G. Lawes and A. K. Tyagi, *J. Phys. Chem. C*, 2013, **117**, 2382 – 2389.
22. A. A. Belik, A. M. Abakumov, A. A. Tsirlin, J. Hadermann, J. Kim, G. V. Tendeloo and E. T. –Muromachi, *Chem. Mater.*, 2011, **23**, 4505 – 4514.
23. J. Zhao, X. Zhang, S. Liu, W. Zhang and Z. Liu, *Journal of Alloys and Compounds*, 2013, **557**, 120 – 123.
24. R. Guo, L. Fang, W. Dong, F. Zheng and M. Shen, *J. Phys. Chem. C*, 2010, **114**, 21390 – 21396.
25. G. S. Lotey and N. K. Verma, *J. Nanopart. Res.*, 2012, **14**, 742.
26. G. L. Bras, D. Colson, A. Forget, N. G. –Riondet, R. Tourbot and P. Bonville, *Phys. Rev. B*, 2009, **80**, 134417.
27. P. Mandal, A. Iyo, Y. Tanaka, A. Sundaresan and C. N. R. Rao, *J. Mater. Chem.*, 2010, **20**, 1646 – 1650.
28. D. P. Dutta, O. D. Jayakumar, A. K. Tyagi, K. G. Girija, C. G. S. Pillai and G. Sharma, *Nanoscale*, 2010, **2**, 1149 – 1154.

29. H. Singh and K. L. Yadav, *J. Phys.: Condens. Matter*, 2011, **23**, 385901.
30. B. Yu, M. Li, J. Liu, D. Guo, L. Pei and X. Zhao, *J.Phys. D: Appl. Phys.*, 2008, **41**, 065003.
31. R. Das, T. Sarkar and K. Mandal, *J. Phys. D: Appl. Phys.*, 2012, **45**, 455002.
32. M. S. Bernardo, T. Jardiel, M. Peiteado, F. J. Mompean, M. G. – Hernandez, M. A. Garcia, M. Villegas and A. C. Caballero, *Chem. Mater.*, 2013, **25**, 1533 – 1541.
33. J. Wei, R. Haumont, R. Jarrier, P. Berhtet and B. Dkhil, *Appl. Phys. Lett.*, 2010, **96**, 102509.
34. X. Qi, J. Dho, R. Tomov, M. G. Blamire and J. L. MacManus-Driscoll, *Appl. Phys. Lett.*, 2005, **86**, 062903.
35. D. Kothari, V. R. Reddy, A. Gupta, V. Sathe, A. Banerjee, S. M. Gupta and A. M. Awasthi, *Appl. Phys. Lett.*, 2007, **91**, 202505.
36. C. –H. Yang, J. Seidel, S. Y. Kim, P. B. Rossen, P. Yu, M. Gajek, Y. H. Chu, L. W. Martin, M. B. Holcomb, Q. He, P. Maksymovych, N. Balke, S. V. Kalinin, A. P. Baddorf, S. R. Basu, M. L. Scullin and R. Ramesh, *Nature Mater.*, 2009, **8**, 485 – 493.
37. D. M. Smyth, *Ann. Rev. Mater.*, 1985, **15**, 329 – 357.
38. C. L. – Pueyo, S. Dilger, M. R. Wagner, M. Gerigk, A. Hoffmann and S. Polarz, *CrystEngComm.*, 2014, DOI: 10.1039/C3CE41670D.
39. M. K. Shobana, *Journal of Physics and Chemistry of Solids*, 2012, **73**, 1040 – 1043.
40. M. M. Seikh, T. Sarkar, V. Pralong, V. Caignaert and B. Raveau, *J. Appl. Phys.*, 2013, **113**, 053910.
41. D. Bochenek, P. Kruk, R. Skulski and P. Wawrzala, *J. Electroceram.*, 2011, **26**, 8 – 13.

42. D. S. Jeong, R. Thomas, R. S. Katiyar, J. F. Scott, H. Kohlstedt, A. Petraru and C. S. Hwang, *Rep. Prog. Phys.*, 2012, **75**, 076502.
43. Y. Yang and W. Lu, *Nanoscale*, 2013, **5**, 10076.
44. D. B. Strukov and H. Kohlstedt, *MRS Bulletin*, 2012, **37**, 108 – 114.
45. A. Sawa, *Materials Today*, 2008, **11**, 28 – 36.
46. J. M. Luo, S. P. Lin, Y. Zheng and B. Wang, *Appl. Phys. Lett.*, 2012, **101**, 062902.
47. C. Wang, K. – J. Jin, Z. –t. Xu, L. Wang, C. Ge, H. –b. Lu, H. –z. Guo, M. He and G. –z. Yang, *Appl. Phys. Lett.*, 2011, **98**, 192901.
48. T. Choi, S. Lee, Y. J. Choi, V. Kiryukhin, S. –W. Cheong, *Science*, 2009, **324**, 63 – 66.
49. S. Hong, T. Choi, J. H. Jeon, Y. Kim, H. Lee, H. – Y. Joo, I. Hwang, J. – S. Kim, S. – O. Kang, S. V. Kalinin and B. H. Park, *Adv. Mater.*, 2013, **25**, 2339 – 2343.
50. K. Yin, M. Li, Y. Liu, C. He, F. Zhuge, B. Chen, W. Lu, X. Pan and R. – W. Li, *Appl. Phys. Lett.*, 2010, **97**, 042101.
51. Q. Xu, X. Yuan, Y. Cao, L. Si and D.Wu, *Solid State Communications*, 2012, **152**, 2036 – 2039.
52. Q. Ke, A. Kumar, X. Lou,K. Zeng and J. Wang, *J. Appl. Phys.*, 2011, **110**, 124102.
53. JCPDS database 1999 Powder diffraction file PDF-2 Data Base International Center for Diffraction Data, JCPDS-ICDD (Pennsylvania, PA).
54. F. Kubel and H. Schmid, *Acta Cryst.*, 1990, **B46**, 698 – 702.
55. R. D. Shannon, *Acta Crystallogr.,* 1976, **A32**, 751 – 767.
56. P. M. Woodward, *Acta Crystallogr B*, 1997, **53**, 44 – 66.
57. Goldschmidt tolerance factor $t=(r_A+r_\circ)/\sqrt{2}(r_B+r_\circ)$, where r_A , r_B and $r_\circ$ represent the average ionic radii of A – cation (Bi^{3+}: 1.17, 1.40 Å in 8 and 12 fold coordination

respectively), B – cation (Fe^{3+}:0.645Å in 6 fold coordination, Li^{1+}: 1.40Å in 6 fold coordination) and oxygen (O^{2-}:1.40Å in 6 fold coordination) respectively. Considering 12 fold coordination for A – site, for ideal undistorted perovskite $t = 1$, $0.985 < t < 1.06$ are untilted perovskite and $0.964 < t < 0.985$ shows anti – phase tilted perovskite, while $t < 0.964$ possibly shows both in – phase and anti – phase tilting.

58. H. Fukumura, H. Harima, K. Kisoda, M. Tamada, Y. Noguchi and M. Miyayama, *J. Magn. Magn. Mater.*, 2007, **310**, e367 – e369.
59. P. Hermet, M. Goffinet, J. Kreisel and Ph. Ghosez, *Phys. Rev. B*, 2007, **75**, 220102(R).
60. M. K. Singh, H. M. Jang, S. Ryu and M. –H. Jo, *Appl. Phys. Lett.*, 2006, **88**, 042907.
61. Y. Q. Jia, *J. Solid State Chem.*, 1991, **95**, 184 – 187.
62. Y. Yang, L. G. Bai, K. Zhu, Y. L. Liu, S. Jiang, J. Liu, J. Chen and X. R. Xing, *J. Phys.: Condens. Matter*, 2009, **21**, 385901.
63. G. –S. Susana, A. Fernando, R. Fernando, V. Rafael, G. Jesus, H. Raphael and K. Jens, *Phys. Rev. B*, 2012, **85**, 144109.
64. F. Huang, Z. Wang, X. Lu, J. Zhang, K. Min, W. Lin, R. Ti, T. Xu, J. He, C. Yue and J. Zhu, *Sci. Rep.*, 2013, **3**, 2907.
65. L. Néel, *Ann. Phys.*, 1936, **5**, 232.
66. L. C. R. Néel, *Acad. Sci.*, 1961, **252**, 4075.
67. T. J. Park, G. C. Papaefthymiou, A. J. Viescas, A. R. Moodenbaugh and S. S. Wong, *Nano Lett.*, 2007, **7**, 766 – 772.
68. J. M. D. Coey, *Magnetism and Magnetic Materials*, Cambridge University Press, **2009**, PP 130 – 150.
69. K. L. Livesey, *Phys. Rev. B*, 2010, **82**, 064408 and References therein.

70. J. Nogués, J. Sort, V. Langlais, V. Skumryev, S. Suriñach, J. S. Muñoz and M. D. Baró, *Phys. Rep.*, 2005, **422**, 65 – 117.
71. S. Giri, M. Patra and S. Majumdar, *J. Phys.: Condens Matter*, 2011, **23**, 073201.
72. I. Sosnowska, W. Schäfer, W. Kocklmann, K. H. Andersen and I. O. Troyanchuk, *Appl. Phys. A*, 2002, **74**, S1040.
73. M. M. Kumar, V. R. Palkar, K. Srinivas and S. V. Suryanarayana, *Appl. Phys. Lett.*, 2000, **76**, 2764.
74. Y.-Q. Kang, M.-S. Cao, J. Yuan and X.-L. Shi, *Mater. Lett.*, 2009, **63**, 1344 – 1346.
75. M. M. Shirolkar, C. Hao, S. Yin, M. Li and H. Wang, *Appl. Phys. Lett.*, 2013, **102**, 243501.
76. E. Linn, R. Rosezin, C. Kuegeler and R. Waser, *Nat. Mater.*, 2010, **9**, 403 – 406.
77. G. Dearnaley, A. M. Stoneham and D. V. Morgan, *Rep. Prog. Phys.,* 1970, **33**, 1129.
78. J. J. Yang, M. D. Pickett, X. Li, D. A. A. Ohlberg, D. R. Stewart and R. S. Williams, *Nat. Nanotechnol.*, 2008, **3**, 429–433.
79. M. D. Pickett, D. B. Strukov, J. L. Borghetti, J. J. Yang, G. S. Snider, D. R. Stewart and R. S. Williams, *J. Appl. Phys.*, 2009, **106**, 074508.
80. Y. Shuai, S. Zhou, D. Bürger, M. Helm and H. Schmidt, *J. Appl. Phys.*, 2011, **109**, 124117.

Table 1 Structure parameters obtained from Rietveld refinement of undoped and doped samples.

Lattice parameters	**Average Bond length (Å)**		**Average Bond angle (Å)**		**ω**
		B_1			
a = 5.583 Å	Bi – O	1st : 2.301	Fe – O – Fe	156.1°	12.2°
		2nd : 2.212			
		Δ (1st – 2nd) = 0.089			
c = 13.880 Å	Fe – O	1st : 2.184	O – Bi – O	73.67°	
		2nd : 1.992			
		Δ (1st – 2nd) = 0.192			
V = 374.68 Å^3					
		B_2			
a = 5.579 Å	Bi – O	1st : 2.323	Fe – O – Fe	155.05°	12.5°
		2nd : 2.216			
		Δ (1st – 2nd) = 0.107			
c =13.859 Å	Fe – O	1st : 2.155	O – Bi – O	73.9°	
		2nd : 1.989			
		Δ (1st – 2nd) = 0.166			
V = 373.57 Å^3					
		B_3			
a = 5.572 Å	Bi – O	1st : 2.378	Fe – O – Fe	153.13°	12.9°
		2nd : 2.221			
		Δ (1st – 2nd) = 0.157			
c =13.838 Å	Fe – O	1st : 2.123	O – Bi – O	74.23°	
		2nd : 1.984			
		Δ (1st – 2nd) = 0.139			
V = 372.07 Å^3					
		B_4			
a = 5.561 Å	Bi – O	1st : 2.405	Fe – O – Fe	151.1°	13.5°
		2nd : 2.230			
		Δ (1st – 2nd) = 0.175			
c =13.803 Å	Fe – O	1st : 2.115	O – Bi – O	74.55°	
		2nd :1.995			
		Δ (1st – 2nd) = 0.120			
V = 369.67 Å^3					

Table 2 Deconvoluated Raman modes for undoped and doped $BiFeO_3$ samples.

Raman modes	Raman shift (cm^{-1})			
	B_1	**B_2**	**B_3**	**B_4**
A_1-1	145	149	153	158
A_1-2	175	177	180	185
A_1-3	227	230	232	236
A_1-4	432	436	440	447
E	77	80	82	86
E	128	131	133	139
E	283	288	292	299
E	295	298	303	309
E	356	358	362	369
E	376	379	382	388
E	479	483	488	493
E	528	533	536	540
E	630	633	637	643

Figure captions

Figure 1 Rietveld refined XRD patterns of undoped and doped samples. The intensity was normalized for the plotting purpose.

Figure 2 Reciprocal space two dimensional electron density plot of BFO unit cell in undoped and doped cases. The black dotted line indicates single FeO_6 octahedra and solid line brown colored circle indicate buckling of FeO_6 octahedra.

Figure 3 Deconvoluated Raman spectra of all $BiFeO_3$ samples. The inset shows magnified view of selected range representing doping percentage dependent red shift and broadening of E modes representing changes in the FeO_6 octahedral environment.

Figure 4 TEM micrographs of as prepared undoped and doped $BiFeO_3$ samples. The inset shows HRTEM micrograph of the single particle.

Figure 5 Room temperature M – H study on undoped and doped samples. The first inset (upper) shows zoomed view of a selected range of magnetic field, representing coercivity, exchange bias field. The second inset (lower) shows the variation of magnetic moment per Fe atom, exchange bias with doping percentage.

Figure 6 Schematic representation of possible mechanism for observed magnetic properties.

Figure 7 Room temperature P - E loop measurement showing doping induced enhanced ferroelectric nature of material. The inset shows relation between doping concentration and polarization parameters.

Figure 8 The resistive switching behavior of $BiFeO_3$ nanoparticles. (A) Schematic of the device with I – V setup for the BRS/CRS experiment. (B) Observed BRS operation for successive 10 cycles. (C), (D) BRS operational stability of the device $Ag/B_4/Cu$ for 10^3 cycles and 10^6 seconds.

(E) CRS 1 bit operation of the device constructed with sample B_4 for consecutive 50 cycles. (F) Voltage pulse mediated 1-bit CRS operation of the device for 10^3 cycles.

Figure 1

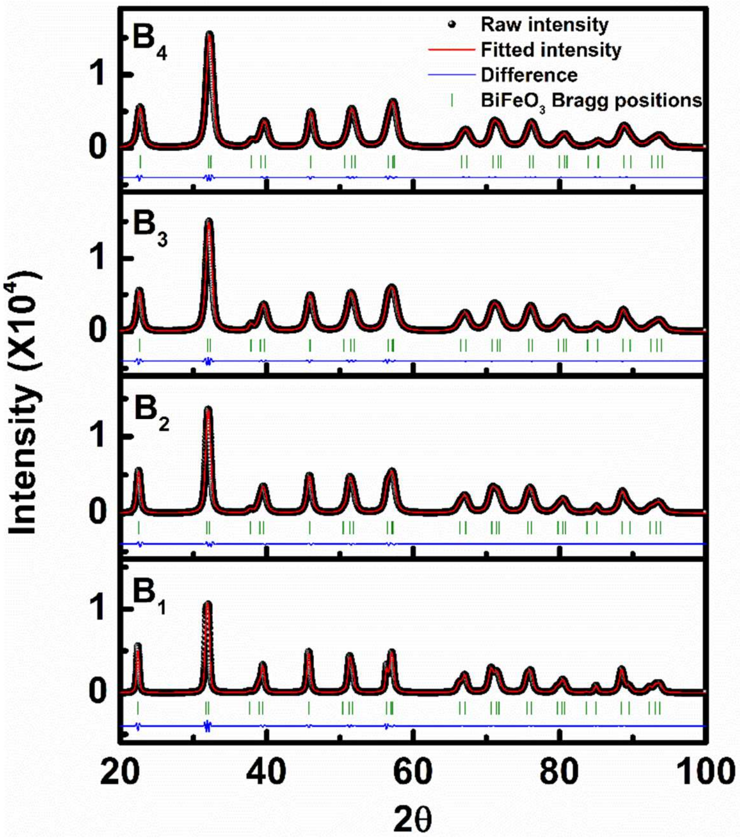

B4
B3
B2
B1
Raw intensity
Fitted intensity
Difference
BiFeO3 Bragg positions
Intensity (X10^4)
0
1
20
40
60
80
100
2θ

Figure 2

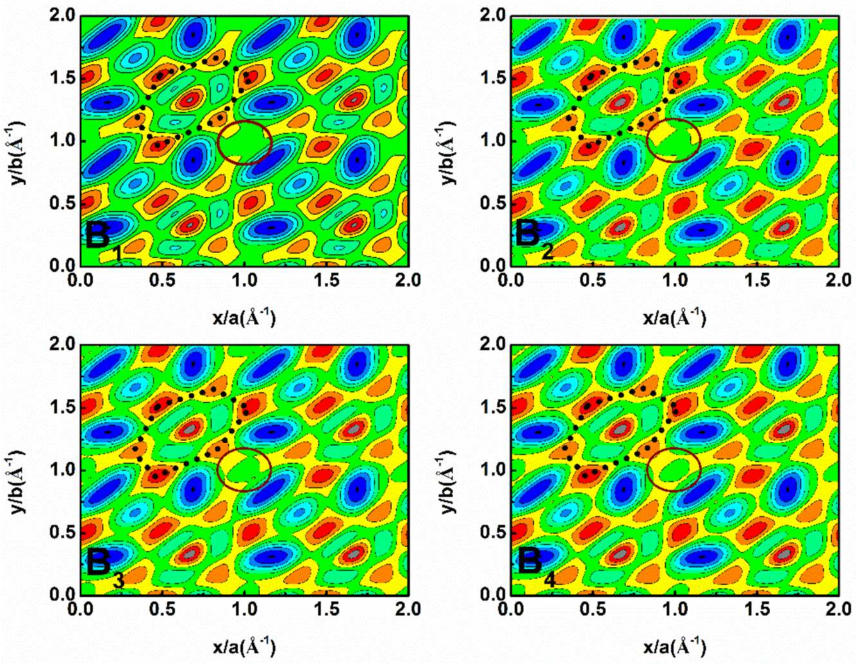

Figure 3

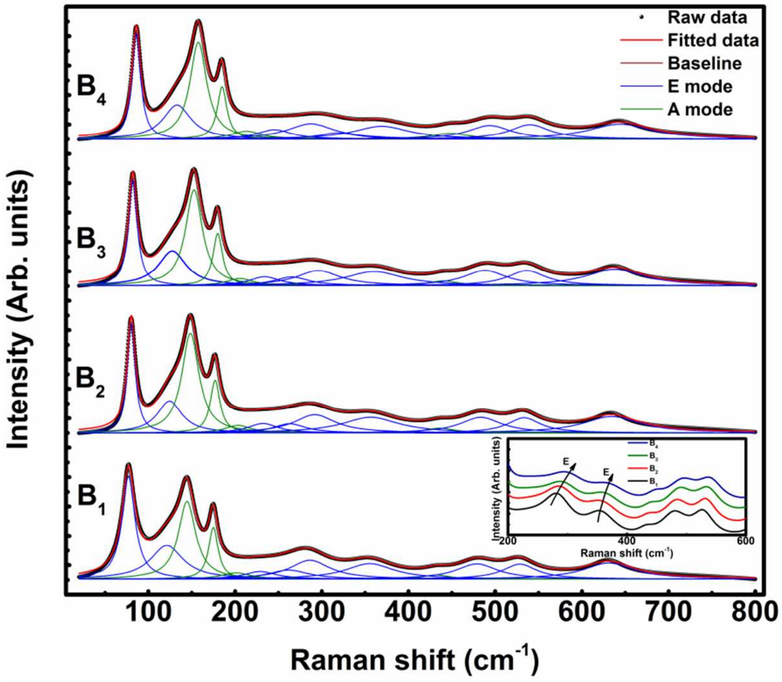
Raw data
Fitted data
Baseline
E mode
A mode
B_4
B_3
B_2
B_1
Intensity (Arb. units)
100
200
300
400
500
600
700
800
Raman shift (cm^{-1})
Intensity (Arb. units)
E
E
B_4
B_3
B_2
B_1
200
400
600
Raman shift (cm^{-1})

Figure 4

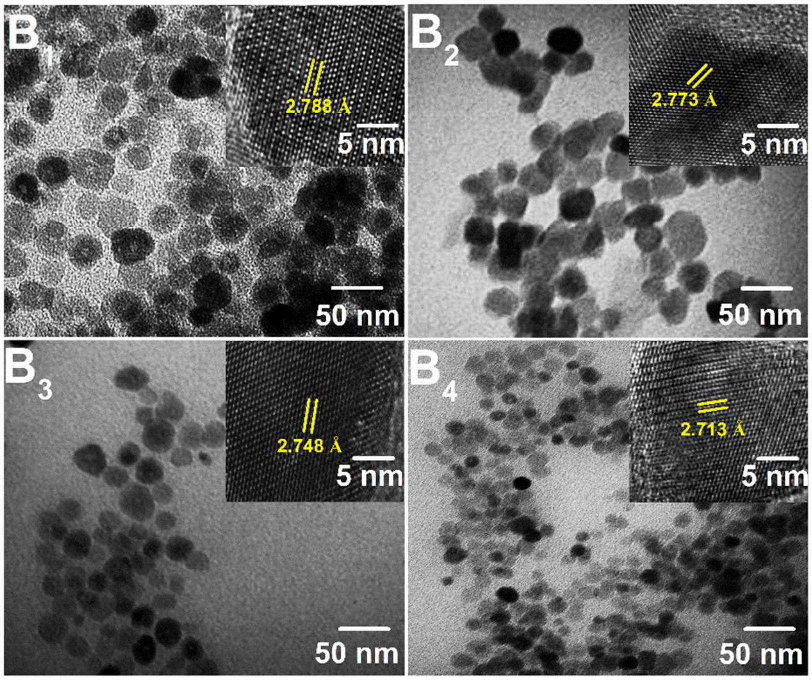
B1
2.788 Å
5 nm
50 nm
B2
2.773 Å
5 nm
50 nm
B3
2.748 Å
5 nm
50 nm
B4
2.713 Å
5 nm
50 nm

Figure 5

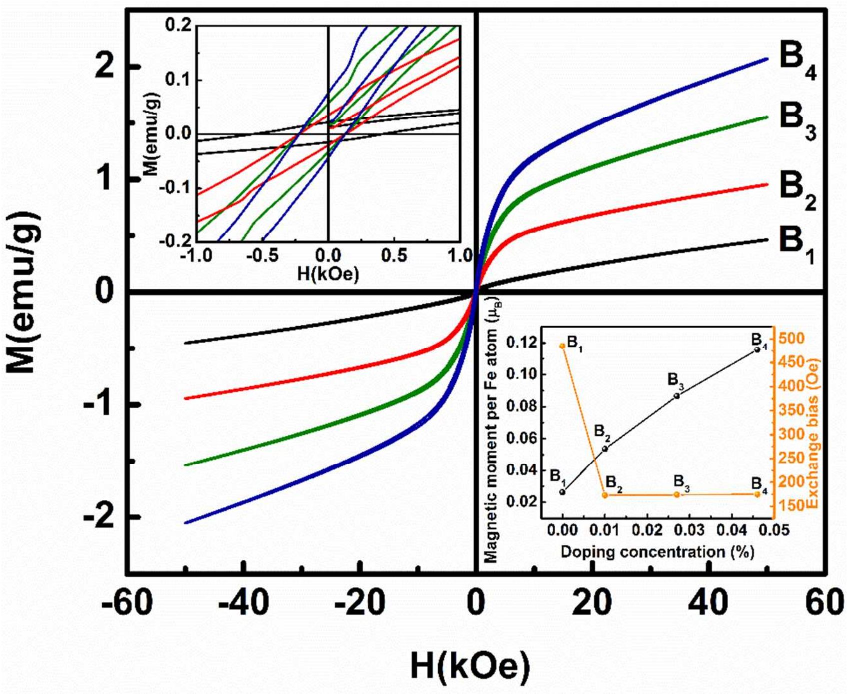
M(emu/g)
H(kOe)
-60
-40
-20
0
20
40
60
2
1
0
-1
-2
B_4
B_3
B_2
B_1
M(emu/g)
H(kOe)
0.2
0.1
0.0
-0.1
-0.2
-1.0
-0.5
0.0
0.5
1.0
Magnetic moment per Fe atom (μ_B)
Exchange bias (Oe)
Doping concentration (%)
0.12
0.10
0.08
0.06
0.04
0.02
500
450
400
350
300
250
200
150
0.00
0.01
0.02
0.03
0.04
0.05
B_1
B_2
B_3
B_4

Figure 6

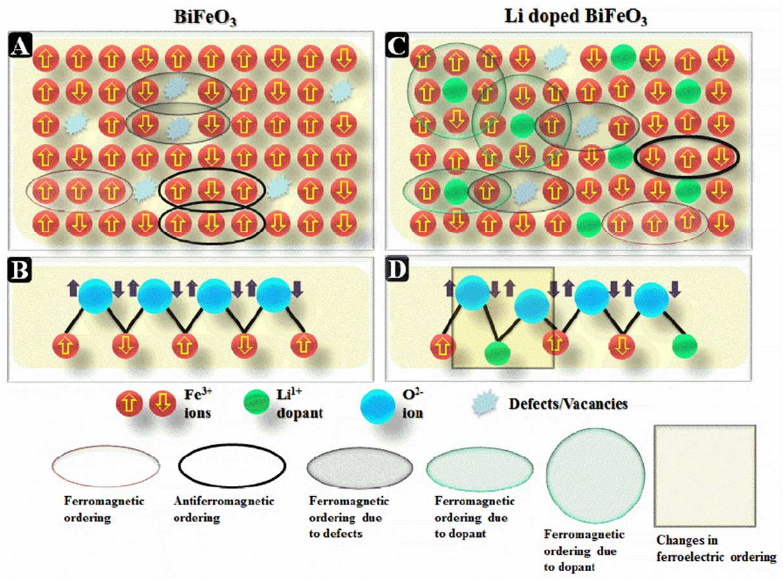
BiFeO$_3$
Li doped BiFeO$_3$
A
B
C
D
Fe^{3+} ions
Li^{1+} dopant
O^{2-} ion
Defects/Vacancies
Ferromagnetic ordering
Antiferromagnetic ordering
Ferromagnetic ordering due to defects
Ferromagnetic ordering due to dopant
Ferromagnetic ordering due to dopant
Changes in ferroelectric ordering

Figure 7

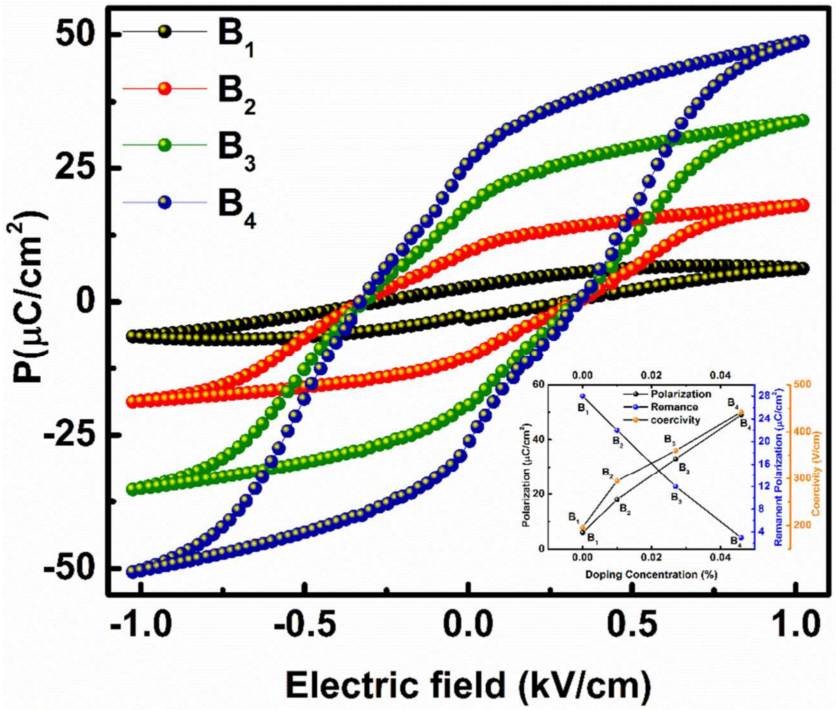
B1
B2
B3
B4
50
25
0
-25
-50
P(μC/cm²)
-1.0
-0.5
0.0
0.5
1.0
Electric field (kV/cm)
Polarization
Remance
coercivity
Polarization (μC/cm²)
Remanent Polarization (μC/cm²)
Coercivity (V/cm)
Doping Concentration (%)
0.00
0.02
0.04
60
40
20
28
24
20
16
12
8
4
500
400
300
200

Figure 8

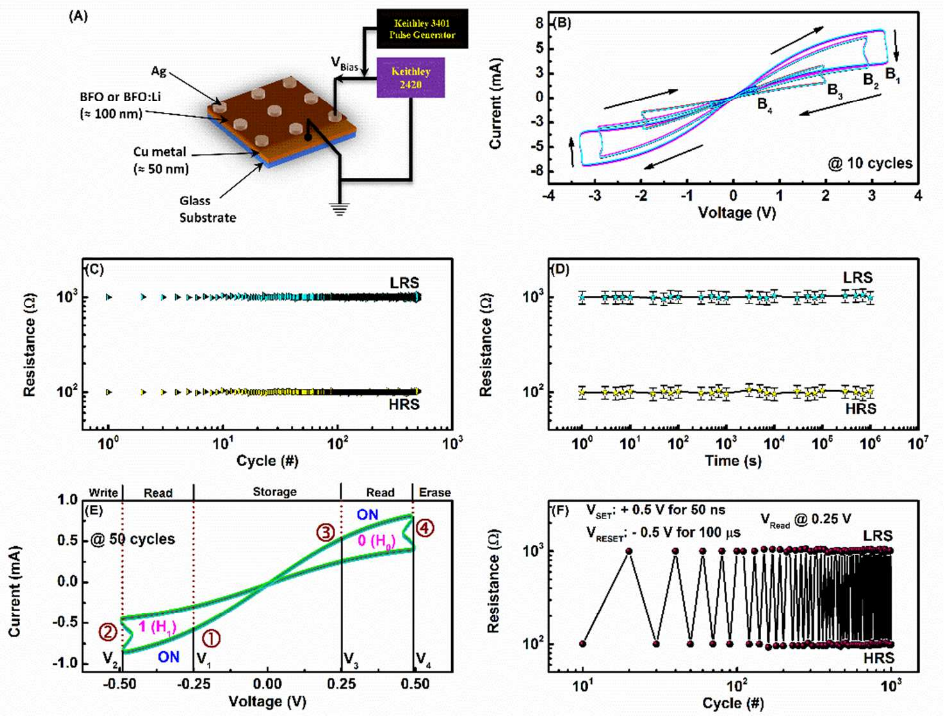
(A)
Keithley 3401 Pulse Generator
Keithley 2420
V_{Bias}
Ag
BFO or BFO:Li (≈ 100 nm)
Cu metal (≈ 50 nm)
Glass Substrate
(B)
Current (mA)
Voltage (V)
B_1
B_2
B_3
B_4
@ 10 cycles
(C)
Resistance (Ω)
Cycle (#)
LRS
HRS
(D)
Resistance (Ω)
Time (s)
LRS
HRS
(E)
Write
Read
Storage
Read
Erase
@ 50 cycles
Current (mA)
Voltage (V)
ON
0 (H_0)
1 (H_1)
ON
①
②
③
④
V_1
V_2
V_3
V_4
(F)
V_{SET}: + 0.5 V for 50 ns
V_{RESET}: - 0.5 V for 100 µs
V_{Read} @ 0.25 V
LRS
HRS
Resistance (Ω)
Cycle (#)

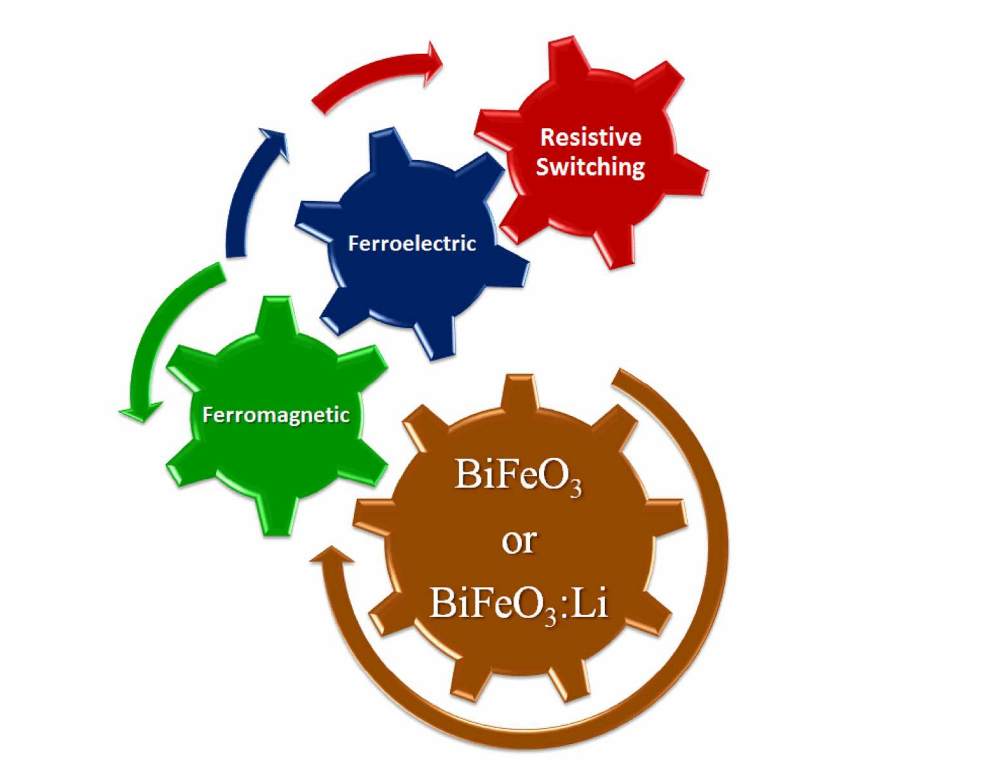

Multiferroic and the resistive switching properties of BiFeO3 nanoparticles were improved by dilute aliovalent Li1+ doping.
207x158mm (300 x 300 DPI)